



The role of filler wire and scanning strategy in laser welding of difficult-to-weld aluminum alloys

Erica Liverani¹ · Alessandro Ascari¹ · Alessandro Fortunato¹

Received: 30 May 2023 / Accepted: 9 July 2023 / Published online: 19 July 2023
© The Author(s) 2023

Abstract

Laser welding of dissimilar aluminum alloys has gained interest over recent years, especially for the production of lightweight components. Pore and crack formation is one of the most critical factors to be taken into consideration for such applications, in particular when one or more parts are produced by die casting or additive manufacturing (AM). Current laser systems offer several methods for defect reduction and process control, while optimized process strategies must be correlated to key factors influencing welding outcomes. In light of these aspects, the current paper investigates the welding of AA6082 sheets with AlSi10Mg parts produced by AM in a lap-joint configuration typical of battery housings in the e-mobility industry. Both laser welding with and without filler wire are investigated, along with the potential advantages of using a wobbling scanning strategy, in order to understand the impact of process strategies on weld bead quality. The importance of process parameter optimization is highlighted for all of the employed strategies, with special emphasis on defects, weld bead chemical composition, joint morphology, and dilution between the materials involved. The findings demonstrate that by introducing filler wire and employing active wobbling, highly reflective alloys can be welded correctly (porosity below 1%, equivalent ultimate strength up to 204 MPa) with good tolerance to variations in process parameters, while filler wire can be excluded in high-productivity welding where linear scanning is employed and detailed optimization of process parameters is performed (porosity below 2%, equivalent ultimate strength up to 190 MPa).

Keywords Laser welding · Filler wire · Aluminum welding · Beam oscillation · Additive manufacturing

1 Introduction

The EU Mobility Strategy (EU Commission Communication, 2020) for electric vehicles (EV) addressing the “Green Deal” specifically emphasizes electrification of transport as one of the biggest contributors to prevent global warming and air pollution. The European Green Deal includes a goal to reduce greenhouse gas emissions associated with transportation by 90% by 2050. In particular, the policy aims to put at least 30 million zero-emissions electric vehicles (EVs) on the road in the EU alone by 2030.

Although EVs do not directly contribute to greenhouse gas emissions, there are a number of environmental issues associated with the manufacturing of EVs that must be

resolved. For instance, a report from carbon brief [1] found that approximately half of the emissions from battery production come from manufacturing of the battery systems themselves, with laser material processing (LMP) being a significant contributor. It has been estimated that LMP covers between 60 and 80% of all materials processing applications for EV manufacturing [2], comprising laser cutting, surface ablation/cladding and welding/bonding, as well as laser-based additive manufacturing (AM). Cost, quality, and sustainability are the three main industrial requirements that must be optimized in the manufacturing and assembly of batteries and battery packs and, as a result, the associated laser processes. Firstly, when the cost is taken into account, the European Technology and Innovation Platform has shown that the production of battery packs and electric motors accounts for more than 40% of total investment costs [3]. The weight of the battery enclosure alone accounts for 20% of the pack’s overall weight. Maximizing the strength-to-weight ratio is therefore one of the key challenges for lowering manufacturing costs. Secondly, manufacturers have

✉ Erica Liverani
erica.liverani2@unibo.it

¹ Department of Industrial Engineering (DIN), Alma Mater Studiorum - University of Bologna, viale Risorgimento 2, 40136 Bologna, Italy

set stringent quality targets, aiming to achieve reliability above 99.7% [4]. Current reports indicate that the assembly of a single battery pack requires about 20,000 welds (cell to tab, busbar to busbar, etc.), which adds up to several billion welds per year. This is daunting considering that gigafactories typically produce approximately 6% defective cells and battery modules [5]. System and data analysis methods [6, 7] for defect monitoring and prediction are being developed; however, the first step toward zero-defect production is optimal process conditions. Thirdly, the reduction of waste materials deriving from production is regarded as a sustainable solution to reducing emissions, with this aspect strongly related to quality requirements.

Based on these considerations, aluminum alloys are suitable candidates for the production of critical battery pack components due to their low production cost and high strength-to-weight ratio [8]. Weight and cost reduction can be further optimized through technological advancements in hybrid materials and processes [9]. For instance, rolled aluminum components can be combined with cast alloys processed using die casting or additive manufacturing technologies to maximize the geometric flexibility of module cases (i.e., for cooling optimization) and improve battery efficiency.

However, LMP of aluminum alloys is currently challenging due to the high reflectivity of these alloys in the infrared, the presence of dissolved gas within the solidified structure where die casting is involved, and the propensity for hot cracking. DiMatteo et al. [10] showed that autogenous butt joints comprising dissimilar aluminum alloys can be obtained with good weld strength but with a porosity of around 5%. To overcome this issue, the benefits of filler wire in gap bridging during laser welding of AA5083 alloy have been highlighted [11], with the selection of the proper filler wire composition an important factor in reducing both crack susceptibility and pore formation [12]. The performance of laser welds can therefore be improved by optimizing the melt pool chemical composition, with the choice of the right filler material essential for successful outcomes in conventional laser welding [13].

The use of a multi-layer base material [14] or the addition of alloying elements to the base material [15] have both been described as alternatives for the optimization of remote laser welding where filler wire is not employed. Crack inhibition of susceptible aluminum alloys can also be carried out by incorporating nanoparticles into the weld zone [16, 17]. From a manufacturing process point of view, recent studies have suggested that laser beam oscillation can enhance weld performance by altering the thermal cycle during the process [18]. This method is made possible by employing a scanning welding head and can be fully integrated into the laser welding process, providing flexibility in defining the spatial energy distribution within the weld zone and allowing its expansion

with advantages in terms of melt pool stability. Because the oscillating laser beam causes a more even temperature distribution and a mechanical stirring effect within the melt pool, research has shown that it promotes the development of equiaxed grains in place of columnar dendrites [19]. Several authors have reported a reduction in bubble formation during experiments utilizing laser beam oscillation, leading to lower porosity in the weld bead [20, 21]. This effect has also been confirmed with numerical simulations [22]. In addition, increasing the oscillation width and frequency can result in a more significant mitigation of weld porosity and consequently higher joint strength [23]. Schultz [24] proposed beam oscillation as a means for evenly distributing energy on the tip of the filler wire. For the purposes of improving laser welding, filler wire and laser oscillation can therefore be combined. By employing both techniques, weld formation, grain growth, and the dynamic behavior of fluid in the melt pool can be optimized to improve weld quality in terms of the following: (a) dealing with gaps, misalignments and differences in thickness, (b) reducing pore formation, and (c) reducing crack susceptibility. However, both strategies have disadvantages in terms of industrial implementation. On the one hand, laser beam oscillation greatly extends production times, while on the other, both beam oscillation and filler wire increase the difficulty of managing and maintaining the welding setup, particularly in the case of welding complex geometries with filler wire.

Based on the potential of this approach, this paper presents a comprehensive comparison of different combinations of laser welding setup, including filler wire and beam oscillation, for achieving optimal joint characteristics. Results are focused on determining the feasibility of laser technology for joining thin sheets in a dissimilar configuration. Laser welding was employed to join 2 mm thick commercial AlSi1MgMn (designated 6082-T6) produced by conventional hot rolling to 5 mm thick AlSi10Mg produced by Laser Powder Bed Fusion (LPBF). Metallographic analysis was performed with an optical microscope (OM), while scanning electron microscopy (SEM/FEG-EDS) to characterize the resulting weld bead morphology and microstructure, allowing these characteristics to be correlated with the laser welding configuration. Tensile-shear tests and microhardness analyses were performed to assess the mechanical properties of joints and correlate these with the microstructure, chemical composition, and adopted welding strategy. The obtained results show that welding of aluminum alloy with filler wire and beam wobbling was the best condition over a wide range of process parameters; however, linear welding without filler wire was demonstrated to be a feasible option for high-productivity welding provided that process parameters were precisely defined.

2 Materials and methods

2.1 Production and characterization of AlSi10Mg parts

Commercial AlSi10Mg atomized powder, supplied by Carpenter (Carpenter Additive, Carpenter Technology Corporation, USA), was used for manufacturing of LPBF sheets. The powder was spherical in shape with dimensions in the range of 20–63 μm . A representative SEM micrograph of powder particles is shown in Fig. 1, allowing shape and morphology evaluation to be performed. Image analysis yielded the following aspect ratio percentiles (between the major and minor axes): 1.09 (D10), 1.30 (D50), and 1.80 (D90).

LPBF parts were produced with a SISMA MYS-INT100 system on a cold-build platform with a diameter of 100 mm. All samples were built in a nitrogen environment with a residual oxygen content $< 0.1\%$ using the same laser parameters, summarized in Table 1, which had been optimized in previous studies [25]. After printing, a stress relief heat treatment was performed at 300 $^{\circ}\text{C}$ with a holding time of 120 min, followed by slow cooling in accordance with the literature [26]. For preliminary base material characterization, tensile test samples were printed with geometry in line with relevant standards (BS EN ISO 4136:2011), having the following main dimensions: 60 mm gauge length, 6 mm width, and 2 mm thickness. Tensile tests were carried out using a hydraulic testing machine (Italsigma S.r.l, Forlì, Italy) with a 20 kN load cell. The strain rate was set to $2.8 \cdot 10^{-4} \text{ s}^{-1}$ and maintained constant using a constant crosshead separation rate of 1 mm/min, as

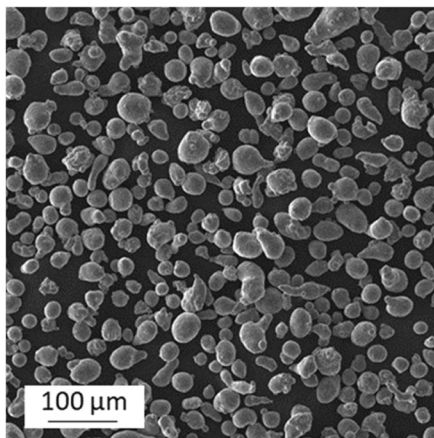


Fig. 1 AlSi10Mg power morphology for LPBF sheet production

Table 1 LPBF process parameters used for sample manufacturing

Laser power (W)	Scan speed (mm/s)	Layer thickness (μm)	Hatch space (μm)	Scan strategy	Support category
175	500	20	70	$3 \times 3 \text{ mm}^2$ roto-translating chess-board	Wall

required by the tensile testing standard (ISO 6892-1). Strain measurements were acquired with a longitudinal extensometer (HBM Type DD1, 2.5mV/V).

2.2 Laser welding

Lap-joint welding of rolled AA6082 (wt%: Cr $\leq 0.25\%$, Fe $\leq 0.5\%$, Mg 0.6–1.2%, Mn 0.4–1%, Si 0.7–1.3%, other elements $< 0.2\%$, Al balance) and the aforementioned LPBF AlSi10Mg sheets was performed to define the optimum welding configuration. Four different conditions were tested, employing linear laser motion (y direction in Fig. 2a) and beam wobbling with and without filler wire. In all configurations, $50 \times 50 \times 1.5 \text{ mm}$ AA6082 sheets were placed on top of $50 \times 50 \times 4 \text{ mm}$ AlSi10Mg sheets with a 45° inclination with respect to z in the x-z plane of the welding head to achieve a weld bead in the corner. The equipment employed for welding included an IPG YLS-6000 fiber source equipped with D50 two-axis scanning optics (see Table 2 for complete characteristics).

The wire feed system was based on a Fronius KD7000 push-pull system with a maximum feed rate of 10 m/min. Welding optics were mounted on a Yaskawa-Motoman HP-20 6-axis anthropomorphic robot.

Shielding gas was a mixture of 15% He and 85% Ar with a flow rate of 30 L/min. Filler wire was AA5356 with a diameter of 1.2 mm. The filler wire guiding nozzle was in a leading configuration with a 30° inclination with respect to y, in y-z plane (Fig. 2a). In order to ensure that samples were in the correct position and a zero gap was obtained, a clamping device was designed and placed beneath the scanning optics.

Table 3 provides a summary of the various process parameters used during the experiments, with the following process parameters varied for optimization: filler material, laser motion, laser power, welding speed, wire speed, and wobbling frequency.

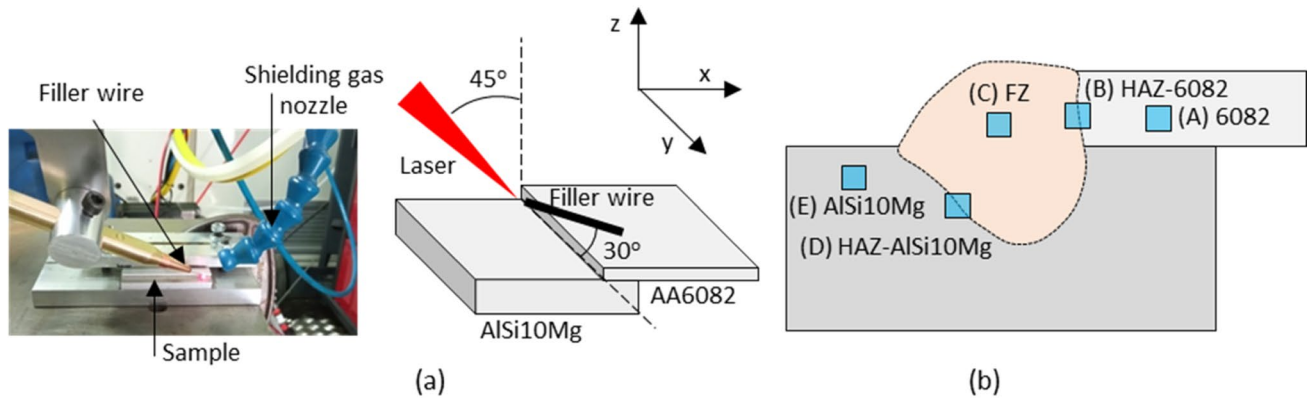


Fig. 2 (a) Experimental setup and (b) key regions considered for microanalysis and microhardness measurements

Table 2 Characteristics of laser source and optics

Maximum power	6 kW
BPP	4 mm
Collimation focal length	200 mm
Focalization focal length	300 mm
Magnification factor	1.5
Fiber core diameter	100 μm
Spot diameter	150 μm
Maximum wobbling frequency	350 Hz

2.3 Microstructural and micro-elemental analysis

Middle cross-sections of the welded samples were prepared by hot mounting samples in resin and polishing the final surface with 800–2500 grit SiC followed by 1–0.05 μm alumina in suspension. Samples for

microstructural analysis were then etched with Keller's reagent (1 ml HF, 1.5 ml HCL, 2.5 ml HNO₃, and 95 ml H₂O) for 20 s to prepare them for initial examination. The primary geometric characteristics of the weld bead were assessed using optical microscopy (OM, Nikon Optiphot-100), with the average porosity determined via image processing using ImageJ open-access software. A SEM-FEG microscope (Tescan Mira3 with Schottky emitter) with EDS system (Bruker X-Flash 630M) for micro-elemental analysis was then used to conduct extensive microstructural tests. As shown in Fig. 2b, the chemical composition of selected samples was evaluated in different weld bead regions, including the base materials (A, E), heat-affected zone—fused zone (HAZ-FZ) interface (B, D) and fused zone (FZ) (C). AlSi10Mg, AA6082, and wire (where present) dilution were examined to highlight material inhomogeneity in the weld bead for the selected welding configurations.

Table 3 Welding process parameters divided into 4 categories: welding with filler wire and linear motion (FL), welding with filler wire and beam wobbling (FW), welding without filler wire and linear motion (L), and welding without filler wire and beam wobbling (W)

Test	Laser power (kW)	Welding speed (mm/s)	Wire speed (m/min)	Wobbling frequency (Hz)	Wobbling amplitude (mm)
Welding with filler wire, linear motion					
1–5 (FL)	2.2–3 every 0.2	25	1.5	/	/
6–10 (FL)		30	1.8		
11–5 (FL)		35	2.1		
1–18 (FL)	2.6	30	1.2, 1.4, 1.6		
Welding with filler wire, wobbling					
1–8 (FW)	As above (see 1–18 FL)			200	1
Welding without filler wire, linear motion					
1–4 (L)	2–2.6 every 0.2	25	/	/	/
5–8 (L)		30			
9–12 (L)		35			
Welding without filler wire, wobbling					
1–3 (W)	2.6	25, 30, 35	/	100	1

2.4 Weld joint mechanical characterization

Vickers microhardness tests were performed on the metallographic samples described in the previous section within the key regions shown in Fig. 2b using a durometer (HX-1000, Remet) with 0.2 kg load (HV0.2) and a dwell time of 10 s. Between six and eight indentations were carried out to analyze the mean hardness of the base materials and the FZ regions, while two indentations were carried out in the HAZ-FZ interface regions following the interface curve, with one below the other. Mechanical characterization with a monoaxial load was performed after contouring the welded samples to achieve a total length of 80 mm, overlap of 10 mm, and width of 25 mm. The equipment used for these tests was described in the laser welding section.

3 Results

3.1 AISi10Mg mechanical properties

Figure 3 compares representative room temperature tensile test curves for as-built and stress-relieved LPBF AISi10Mg samples. Figure 4a reports the mechanical properties obtained from curve analysis in terms of mean yield stress, tensile strength, and elongation. Figure 4b instead displays the Young’s modulus, resilience, and toughness modulus. There are noticeable differences in the tensile behavior depending on the initial condition of the alloy (as-built or after stress relief). Differences can be observed in relation to both elastic (yield stress, resilience modulus) and plastic (tensile strength, elongation, toughness modulus) properties, as highlighted by the mean values. However, an even more important factor to consider is the standard deviation, which in as-built conditions takes on very high values and provides unstable average data,

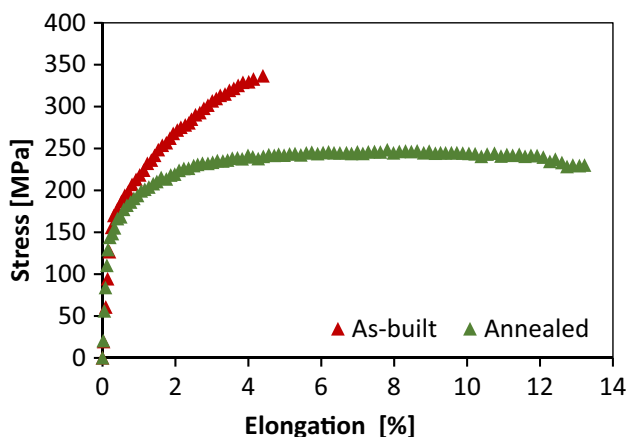


Fig. 3 Representative tensile test curves for the as-built and heat-treated LPBF AISi10Mg alloy

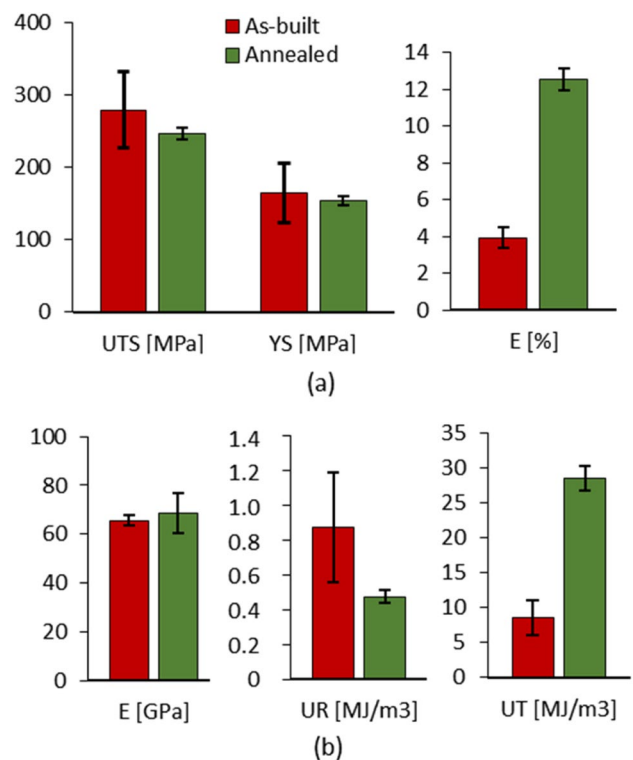


Fig. 4 a Yield stress, tensile strength, elongation to failure, and b Young’s modulus, resilience modulus and toughness modulus obtained from tensile tests for as-built and heat-treated LPBF AISi10Mg alloy

particularly in relation to the elastic behavior. If heat treatment is applied, this value drastically decreases, implying that the observed variability is due to the microstructure rather than the occurrence of internal defects. Upon more detailed assessment of outcomes in terms of yield stress, the heat-treated alloy achieved a value of $R_{p0.2} = 154 \pm 7$ MPa, which is comparable to samples produced under similar conditions (in particular without platform pre-heating) in the literature [27]. Similar considerations can also be drawn for the ultimate tensile strength, with the same samples achieving a value of $R_m = 247 \pm 4$ MPa. In terms of elongation to failure, equal to $A\% = 12.5 \pm 1.2\%$, the heat-treated alloy was characterized by overall satisfactory mechanical behavior, comparable to the conventional die-cast alloy. This condition was therefore selected for subsequent welding experiments.

Furthermore, despite stress relief leading to a decrease in resilience modulus, implying a decrease in the ability of the material to adsorb energy when subject to elastic deformation, it also leads to a significant increase in toughness modulus, implying an increase in energy absorption during plastic deformation. Compared to the as-built state, the reduction in resilience modulus was 54% (0.48 ± 0.07 MJ/m³) while the increase in toughness modulus was 30% (28.6 ± 2.4 MJ/m³). Similar observations can be made to those in

relation to strength but with a much higher standard deviation in the case of as-built samples.

3.2 Welding process optimization

By firstly analyzing welding experiments performed with filler wire, the results presented in Fig. 5a show that certain parameter combinations lead to a weld bead with porosity less than 5% (green area) for both linear (red points) and wobbling (black point) laser scanning. These conditions correspond to parameters with the lowest energy input, which translates to lower power and faster welding speeds. However, linear movement generally leads to higher porosity, with the average value across all tests being 10.6% in the case of linear motion and 6.5% with wobbling. Furthermore, only one parameter set achieved acceptable outcomes in the former case, while six conditions led to porosity below 5% in the latter, further supporting this consideration. The impact of laser motion on weld bead geometry is even more evident, with a lower aspect ratio (weld depth/weld width = D/W) achieved with wobbling (see Fig. 5b). The mean aspect ratio and standard deviation are 0.83 (max = 1.09, min = 0.67) and 0.13, respectively, with linear motion, while wobbling leads to a 54% decrease in terms of mean aspect ratio ($D/W = 0.45$, max = 0.55, min = 0.34), with a standard deviation of 0.06.

As can be observed in the representative micrographs shown in Fig. 5b, both joints exhibit undesired reinforcement. In both cases, different wire speeds were tested to

eliminate this defect while maintaining the same laser power and speed (see tests 15–18 FL and WL in Table 3). Results in terms of reinforcement height with different values of wire speed, from 1.8 to 1.2 m/min, are reported in Table 4 for linear scanning and wobbling. In the case of linear motion, a significant improvement in weld bead geometry was achieved by reducing the wire speed (see Fig. 6a). Samples welded with beam wobbling instead did not exhibit any appreciable improvement (Fig. 6b), with the bead appearing unfilled at lower wire feed rates.

Tests were also performed without filler wire using beam wobbling to improve material dilution during welding. Direct interaction between the laser beam and sheets also allows a wider melt pool to be achieved with linear motion, as shown in Fig. 7a. With beam wobbling, the resulting mean weld aspect ratio is 0.57 (max = 0.64, min = 0.48) with a standard deviation of 0.05, while linear motion leads to values of 0.42 and 0.03, respectively. These

Table 4 Weld bead reinforcement mitigation by reducing wire speed in both linear and wobbling configurations

	REF (1.8 m/ min)	1.6 m/min	1.4 m/min	1.2 m/min
FL reinforcement (mm)	0.63	0.24	< 0.1	< 0.1
FW reinforcement (mm)	0.22	0.18	0.24	Defect

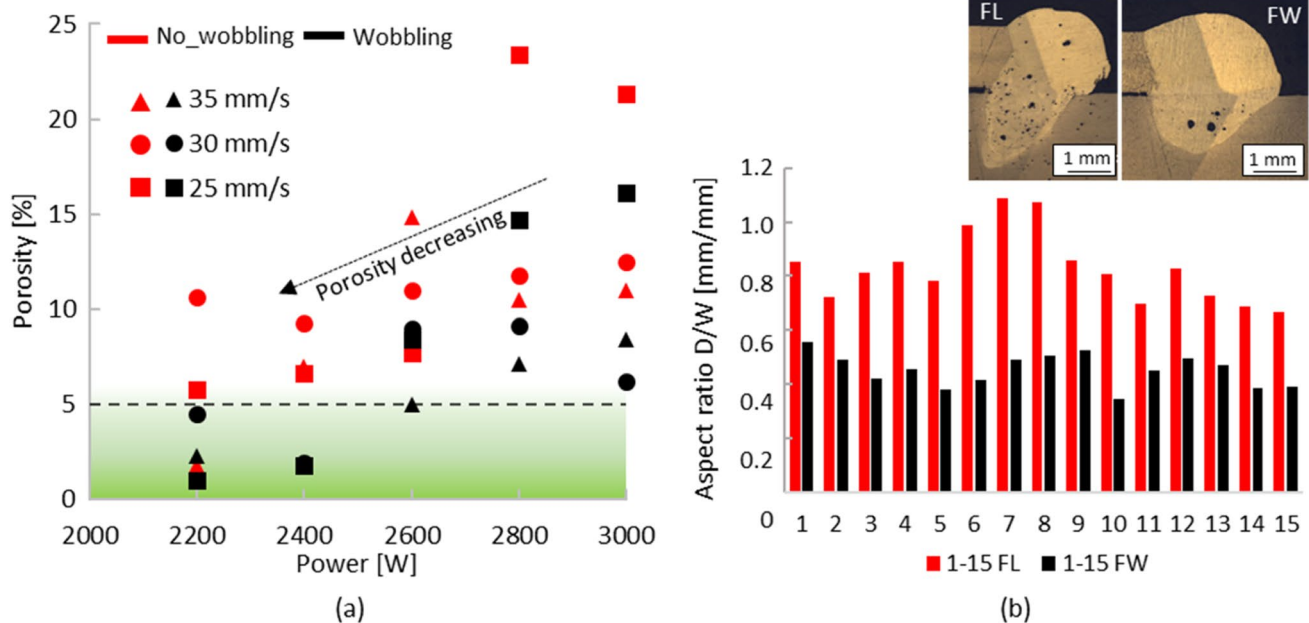


Fig. 5 **a** Measured weld bead porosity after welding with filler wire and linear (red) or wobbling (black) laser motion and **b** weld bead aspect ratio under the same conditions (see Table 3 for correspondence between test number and process parameters)

Fig. 6 Reinforcement reduction by reducing wire speed in FL (a) and FW (b) samples obtained at 1.4 m/min and 1.6 m/min, respectively

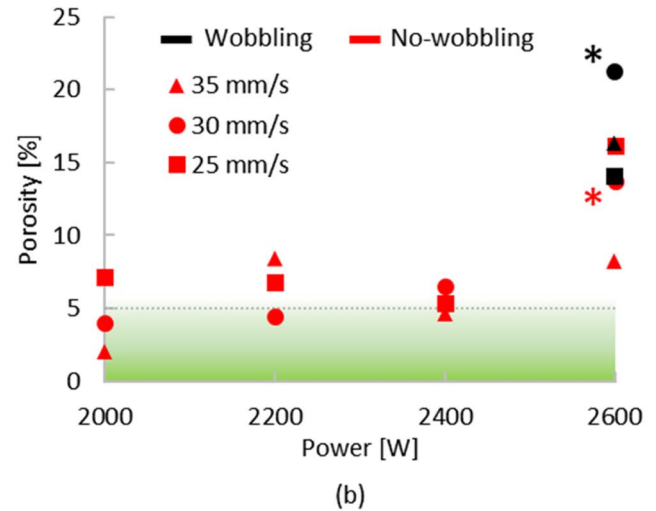
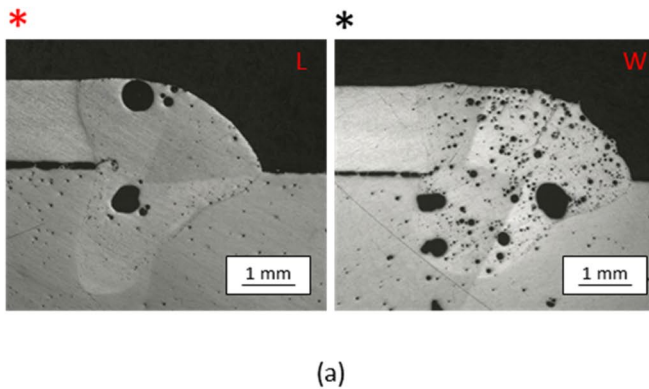
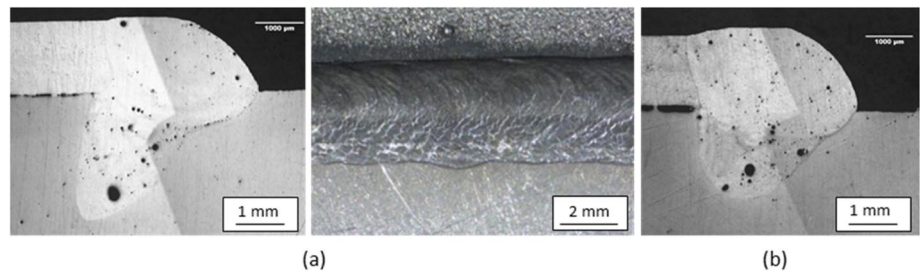


Fig. 7 (a) Weld bead geometry achieved without filler material while employing linear laser scanning (left) and wobbling (right) at the same laser power and speed and (b) weld bead porosity in the same

configurations. Red and black stars indicate parameters employed for welding of samples presented in the micrographs

outcomes confirm the effect of wobbling on weld bead morphology but also highlight the minor contribution of filler wire on the aspect ratio. Without filler wire, activation of wobbling causes an increase in melt pool turbulence, which leads to an increase in porosity without any benefits that can justify its use. By observing the results presented in Fig. 7b, process parameters leading to low porosity can be identified for welds performed with linear motion. As for welding performed with filler wire, lower fluence is required to decrease the detrimental effect of gas entrapment.

Regarding the relationship between weld bead morphology and process variables, Fig. 8 illustrates the variation in joint width with setup and welding speed. The graph highlights how the relationship between joint width and speed remains unchanged in all cases; that is, lower welding speeds lead to larger widths. Figure 8 also supports previous observations in relation to the effect of beam motion on the resulting joint: linear motion with filler wire produces elongated joints, wobbling with filler wire produces flat joints, and exclusion of filler wire causes wider beads with intermediate depths.

3.3 Microstructural and micro-elemental analysis

Based on the obtained outcomes, three optimum samples were used for in-depth microstructural analysis, one for each of the selected welding conditions. Table 5 summarizes the identified process parameters.

Figure 9 shows the microstructure of the 1_FW sample in the regions of interest presented in Fig. 2. Hot rolled 6082 and AlSi10Mg-LPBF sheets were firstly analyzed far from the weld bead in terms of microstructure and chemical composition (see Table 6), after which the FZ-HAZ interface and central FZ region were compared with the base materials. AlSi10Mg sheets after stress relief (see E) were characterized by a homogeneous microstructure with Si particles distributed in the α -Al matrix, while 6082 sheets (see A) exhibited directional deformation of rolled grains with dispersed particles inside.

SEM analyses of the microstructure in the HAZ and FZ are reported in inserts B, C, and D of the same figure. Starting from the HAZ-FZ interface on the AlSi10Mg side (D), the dispersed Si particles start to reticulate into a well-organized eutectic-Si network. Near the border, the

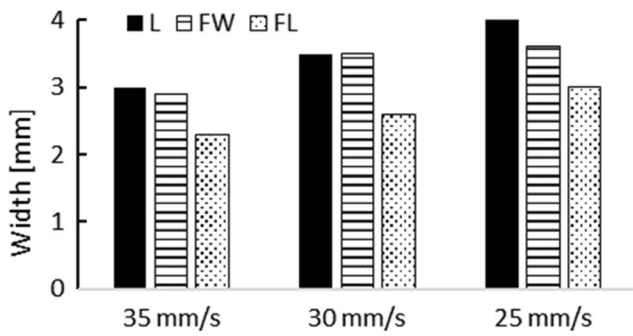


Fig. 8 Weld bead width at different welding speeds for all selected conditions with a constant laser power of 2200 W

Table 5 Optimum welding samples identified for microstructural analysis

Sample welding condition	Laser power (W)	Welding speed (mm/s)	Wire speed (m/min)	Wobbling amplitude (mm) and frequency (Hz)
11_FL	2200	35	2.1	/
1_FW	2200	25	1.5	1_200
9_L	2000	35	/	/

network is interconnected and fine, while further from the melt pool boundary, it becomes coarser and discontinuous. In the middle of the weld bead (C), the network appears to be completely broken, with Si branches surrounded by the Al matrix up to the second FZ-HAZ border (B) with the 6082 sheet, after which no silicon structures are visible.

Figure 10 presents analogous micrographs for the 11_FL and 9_L samples. No significant differences are visible in the former case (11-FL, Fig. 10a) compared to 1_FW, while the Si network in the middle of the joint is more continuous in the latter case (9_L, Fig. 10b) where welding was performed without filler wire.

The chemical composition in each zone was determined via EDS micro-elemental analysis in all regions highlighted within yellow boxes in Figs. 9 and 10 with the aim of obtaining information regarding the chemical anisotropy of the weld bead due to the different base materials, filler wire, dilution methods, and use of beam wobbling or not. Table 6 displays the chemical composition of the base materials, reported in the second and third rows, as mean values obtained from measurements performed on all samples. Data obtained within specific areas of the samples will be analyzed further below.

Figure 11 displays EDS maps of sample 11_FL in both regions D (Fig. 11a) and C (Fig. 11b), supporting the aforementioned observations. The maps confirm the presence of Mg and Si in region C, which are distributed uniformly

Fig. 9 High magnification FEG-SEM micrographs showing the microstructure of the 1_FW sample in the FZ (C) and HAZ regions (B, D) compared to the initial AlSi10Mg (E) and 6082 (A) sheets

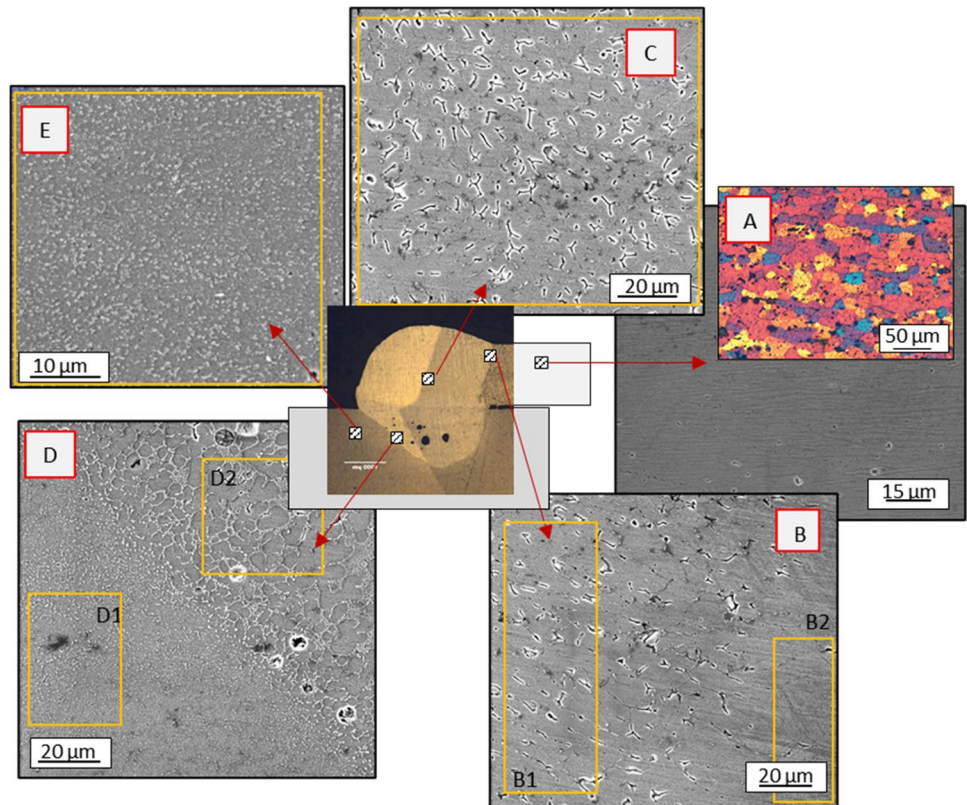


Table 6 Results of SEM-EDS analyses (wt%) performed in the FZ, at the FZ-HAZ interface and on the base material of 1-FW, 11_FL, and 9_L samples

Spectrum	Al	SI	Mg	Fe	Mn	Others
6082 (mean)	Balance	0.62	0.80	< 0.1	0.12	< 0.2
AISI10Mg (mean)	Balance	14.6	0.24	0.27	/	
1_FW						
B1	Balance	3.14	1.04	0.20	/	< 0.2
B2	Balance	0.73	0.81	0.52	/	
C	Balance	3.37	1.22	0.10	/	
D1	Balance	15.2	0.24	0.08	0.15	
D2	Balance	14.4	0.49	0.13	0.03	
11_FL						
C	Balance	2.62	1.28	0.34	0.4	< 0.2
D1	Balance	14.6	0.3	/	0.1	
D2	Balance	13.3	1.0	/	0.1	
9_L						
D1	Balance	14.58	0.22	0.18	/	< 0.2
B1	Balance	9.2	0.43	0.23	0.01	
C	Balance	8.6	0.3	/	0.05	

despite their lower weight percentages. On the contrary, the percentage of Si is higher, but the element is concentrated in the form of network structures in the interface region. On the other hand, magnesium is more prevalent in the FZ zone (D2) than in the HAZ.

3.4 Weld bead mechanical properties

The results of Vickers microhardness tests carried out at the positions indicated in Fig. 2 are reported in Table 7. For the

FW sample, maximum hardness was obtained in the FZ, with a mean value of 112 HV, which was higher than values obtained for both base materials and the FZ of other samples. The FL weld bead hardness was 106 HV, while lower hardness (83 HV) was measured in the L sample without filler wire. The HAZ on the 6082 side exhibited lower hardness than the HAZ on the AISI10Mg side under all conditions, in line with the hardness of both base materials. The difference was up to 40% with filler wire but approximately 10% without. Upon analysis of the data, it became evident

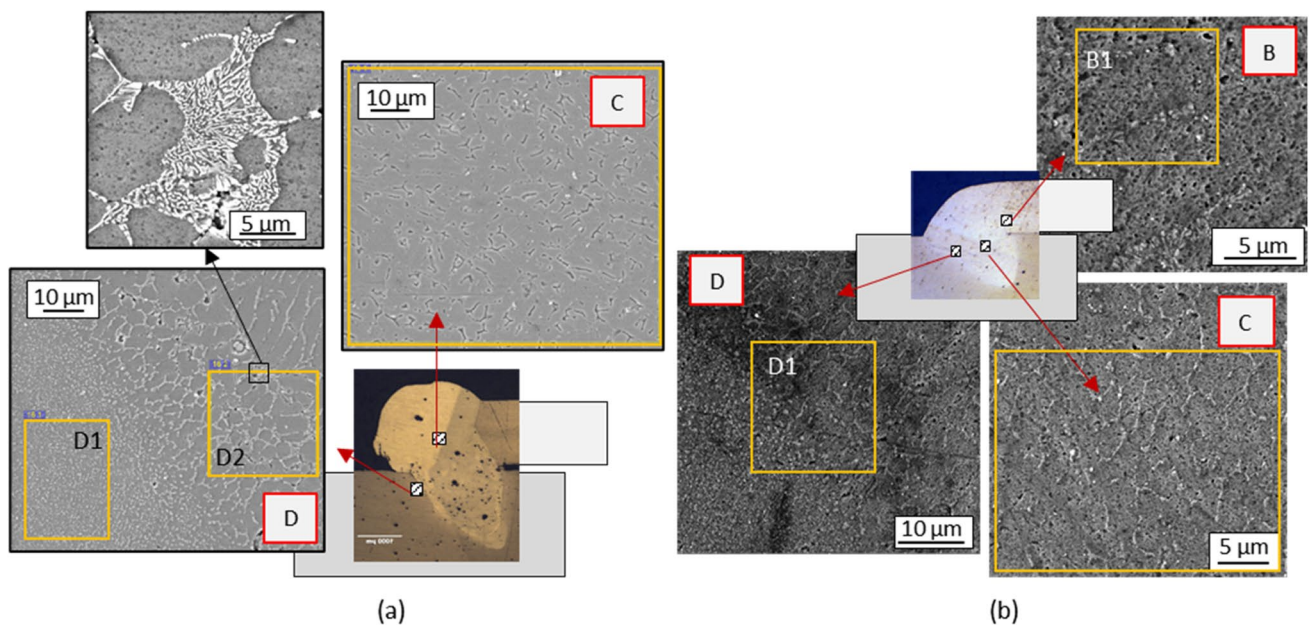


Fig. 10 High magnification FEG-SEM micrographs showing the microstructures of 11_FL (a) and 9_L (b) samples in the FZ (C) and HAZ regions (B, D)

that the presence of filler wire increased the hardness of the melt pool, leading to approximately 30% higher values of hardness for 1_FW and 11_FL samples compared to the 9_L sample. The exclusion of filler wire resulted in comparable hardness in the various regions of interest, with a maximum percentage difference of 11.5%. Samples welded with filler wire instead exhibited higher peak hardness resulting from the chemical composition of the wire, and more significant differences between this value and the hardness obtained within the HAZ.

Finally, tensile-shear tests were performed on samples welded under the same conditions, with three samples tested for each type. The aim was to measure the maximum failure load and equivalent ultimate strength allowing these values to be correlated with the process variables and defects examined previously. Finally, the fracture surface of tested samples was evaluated to determine the occurrence of defects along the entire bead and not just in a single cross-section in order to provide a more complete representation of the weld.

The results of tensile-shear tests were in line with the outcomes of mechanical characterization. 1_FW samples exhibited the highest strength, with a mean failure load of 5.9 kN and a standard deviation of 0.37, followed by 9_L samples, which withstood loads of up to 5.3 kN with a standard deviation of 0.18, and finally, 11_FL samples, which exhibited a mean failure load of 4.8 kN and a standard deviation of 0.14. Fracture took place along the interface between the FZ and AA6082 base material in all cases, indicating relatively low strength of the weld seam borders compared to the central FZ and a concentration of defects along the interface.

Table 7 Measured hardness in weld joint cross-sections: FZ (C), HAZ (B, D), LPBF sheet (AlSi10Mg-E) and rolled sheet (6082-A).

Sample	Region	Hardness (HV0.2)	Standard deviation
All	E	89.5	6.0
	A	60.6	2.0
1_FW	C	112.4	4.8
	B	56.4	/
	D	93.4	/
11_FL	C	105.6	4.4
	B	64.2	/
	D	104.9	/
9_L	C	82.7	2.7
	B	76.1	/
	D	85.1	/

Figure 12 presents representative SEM images of fracture surfaces following tensile-shear tests for samples achieving the highest and lowest weld strength, with 11_FL presented in Fig. 12a and 1_FW presented in Fig. 12b. Both samples are characterized by initial ductile fracture (in the upper part highlighted by the red dashed line), with the presence of small dimples, followed by fragile breakage. However, larger pores are distributed along the entire fracture surface of 11_FL compared to 1_FW, which is characterized by relatively small pores.

Similar considerations can be made in relation to the equivalent ultimate strength. Figure 13 presents the equivalent ultimate strength (US) of the same three

Fig. 11 EDS elemental analysis of sample 11_FL at the HAZ-AlSi10Mg interface (a) and in the FZ (b)

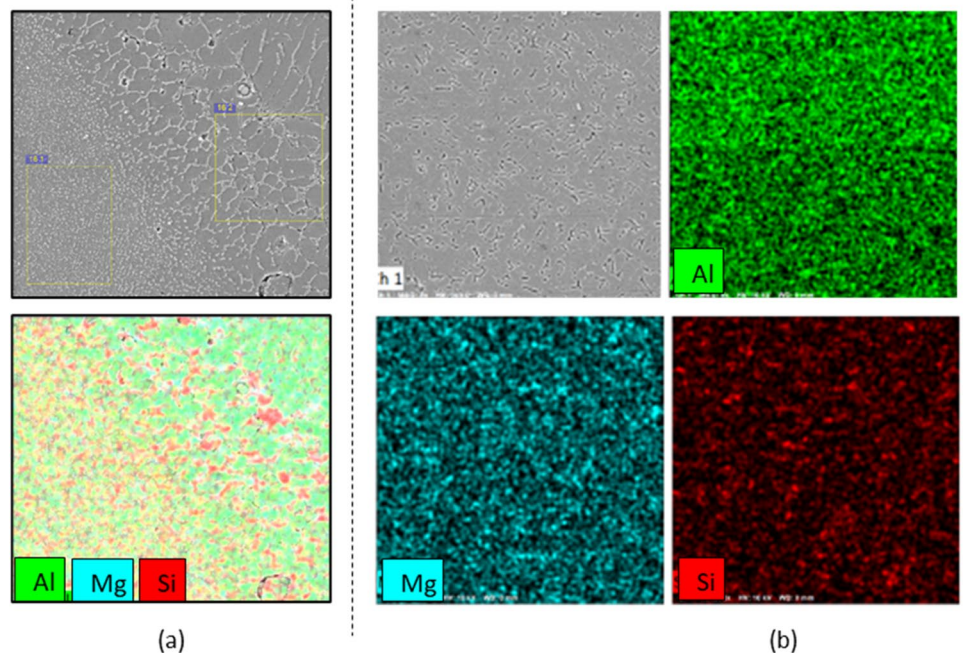
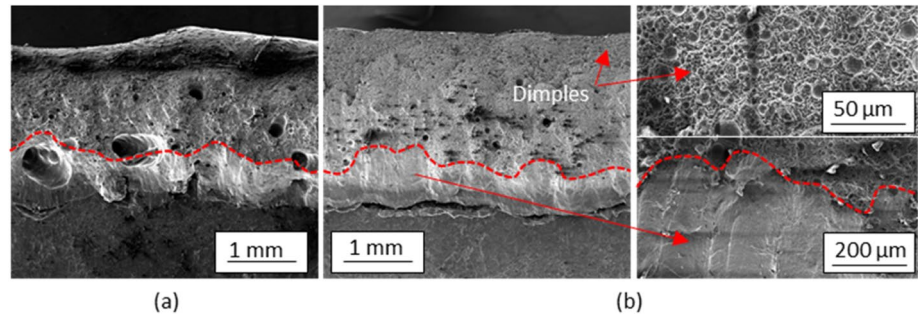


Fig. 12 Fracture surface obtained by SEM analysis of 11_FL (a) and 1_FW samples (b). Magnification of ductile-fragile interface and ductile dimples are shown at the right of 1_FW



samples, where it can be seen that similar values are achieved in each case. 1_FW samples exhibit a higher mean value of US by a factor of 1.07 compared to 9_L samples, which achieve the lowest mean value. When examining the representative stress-displacement curves in Fig. 13b, it can be seen that 1_FW also exhibits more ductile mechanical behavior than the other samples. This finding is supported by the fracture surface analysis described previously. 11_FL and 9_L samples exhibited more brittle welds due to the larger number of pores (see Fig. 13a).

4 Discussion

One of the main issues currently facing laser welding of dissimilar aluminum alloys is the definition of an industry-ready process capable of assuring high-quality joints, geometric flexibility, and good productivity. In view of this, the presented work has determined the feasibility of laser technology to join thin sheets in a dissimilar configuration comprising commercial 6082-T6 sheet produced by

conventional hot rolling with stress-relieved AISI10Mg sheets produced by LPBF. The effects of filler wire, laser motion, and welding parameters were studied in terms of both mechanical properties and microstructure in order to define the best welding conditions available with state-of-the-art laser systems.

4.1 Weld bead morphology and microstructure

All of the tested welding configurations allowed a combination of parameters to be identified that achieved a weld bead porosity of less than 5%, with the exception of linear laser motion without filler wire, which was consequently excluded from subsequent tests. In relation to the weld bead morphology with filler wire, a lower aspect ratio can be achieved by activating wobbling, going from a maximum value of 0.67 with linear motion to a minimum value of 0.34 with wobbling. The main distinction between the two modes is that the bead width is larger when wobbling is activated because the oscillating beam has the effect of “stirring” the molten pool over a larger area. Additionally, wobbling generally results in a decrease in penetration depth. This is because the oscillation of the beam

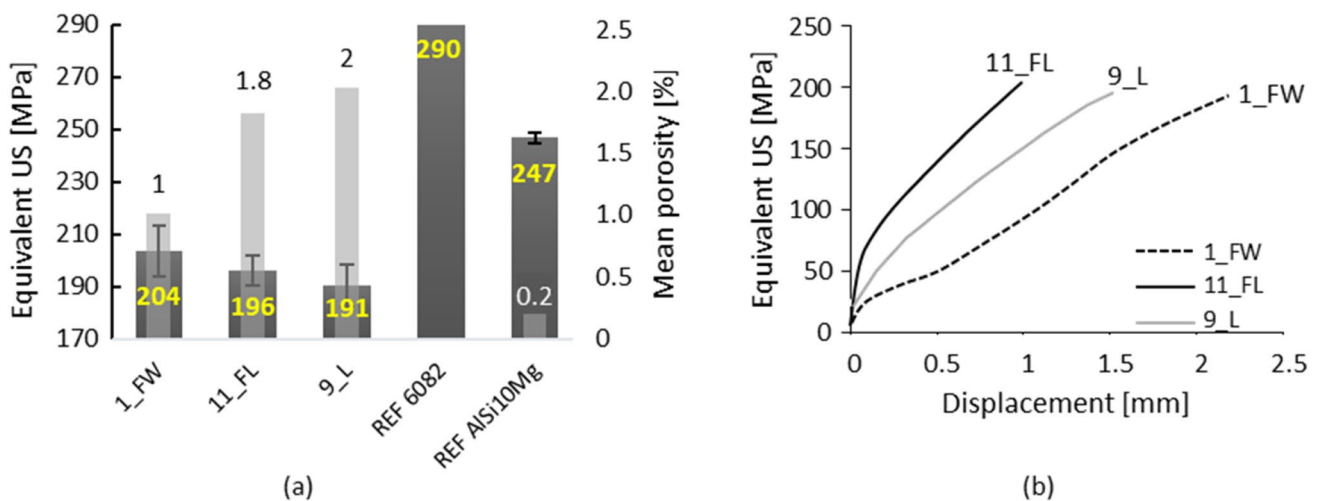


Fig. 13 Results of tensile-shear tests in terms of equivalent ultimate strength: mean values (a) and representative tensile-test curve comparison (b)

expands the area in which interaction between the laser beam and base material takes place, causing a larger molten area to be created and a decrease in energy density throughout the process. Beam wobbling effectively induces a larger apparent spot that widens the melt pool while maintaining a small “instantaneous” spot that promotes good laser-material interaction for highly reflective materials. In relation to the weld bead morphology without filler wire, the aspect ratio takes on intermediate values of 0.57 and 0.42 with and without wobbling, respectively. In general, the weld bead width increases as the welding speed decreases under all conditions due to the increased heat input in terms of linear energy density, which is in alignment with the findings of Sanchez-Amaya et al. [28].

4.2 Welding process parameters

In terms of welding parameters and their relationship to weld quality, increasing the welding speed and/or lowering laser power reduces the size and quantity of pores. These findings are consistent with those of other authors [8, 29], who came to the conclusion that the stability of the melt pool improves and, consequently, the presence of pores decreases during laser beam welding of AlSi10Mg alloys as the weld speed increases, while the average pore size increases with heat input. With this general trend established, the tested process conditions showed that joints with porosity below 5% can be achieved; however, the two contrasting conditions of “wire with wobbling” (FW) and “direct and linear” (L) achieved the lowest mean porosity values, widening the process operating window.

Figure 14 provides an illustration of the aforementioned results, highlighting optimum welding conditions within the gray dashed box and displaying representative micrographs of weld bead morphology and defects under various process conditions.

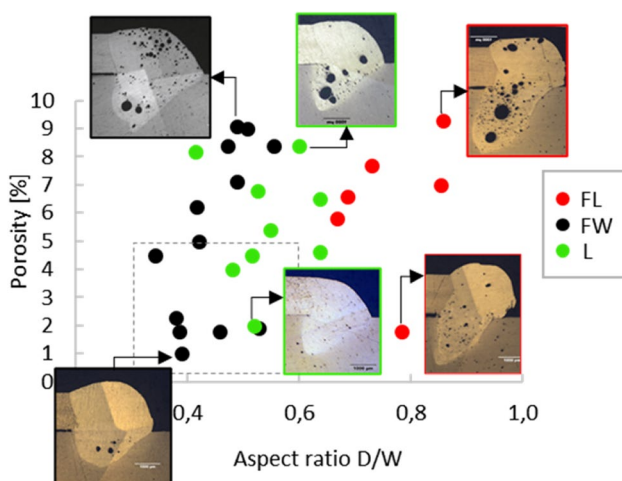


Fig. 14 Porosity vs. aspect ratio of joints obtained under all tested conditions. Optimum welding conditions show in gray dashed box

4.3 Microstructure and chemical composition of weld bead

SEM/FEG analysis highlighted the microstructures of the weld beads in various positions. Starting with LPBF AlSi10Mg, microscopy revealed an interrupted network of Si with the coalescence of very small globular Si particles, with some in the range 1–2 μm but most below 1 μm . Continuing toward the HAZ-AlSi10Mg interface, a fine cellular structure comprising an uninterrupted network of eutectic Si surrounding the Al- α phase was observed (Fig. 15). This network grows from the HAZ to the FZ, with equiaxed grains becoming columnar due to the directional solidification typical of laser welding. The highest temperature gradient is in the welding direction, with dendrites consequently growing into elongated grains in the direction of the heat flux [30]. Moving to the center, the Si-rich network broke up giving way to silicon branches that gradually dissolved in the vicinity of the HAZ-6082 interface.

Despite the general microstructural characteristics of all samples being the same, some relevant differences were highlighted via EDS micro-elemental analysis. Based on the detailed analysis of data reported in Table 6, several remarks can be made in relation to these results:

- AlSi10Mg-LPBF contains a higher percentage of Si, as expected (the nominal value is 9–11%).
- The FZ-HAZ boundary on the AlSi10Mg side, both inside the FZ and HAZ (E1 and E2 in Fig. 9), maintains a high percentage of Si, comparable with that of the base material.
- The FZ-HAZ boundary on the 6082 side exhibits a marked effect of material dilution. Inside the FZ side of region B (B1), the Si percentage takes on an intermediate value between that of AlSi10Mg,

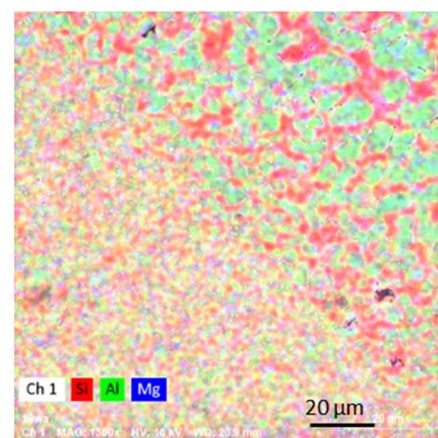


Fig. 15 Elemental analysis of AlSi10Mg and HAZ-AlSi10Mg interface (map from 1_FW EDS micro-elemental analysis)

the filler wire and 6082. This implies a significant presence of AlSi10Mg inside the melt pool during welding, more so than 6082.

- Both samples welded with the addition of filler wire, 1_FW and 11_FL, exhibit intermediate percentages of Si within the FZ region, 3.37% and 2.62% respectively, highlighting the effect of the low-Si wire.
- If the filler wire is excluded, the percentage of Si inside the FZ increases up to 8.6%, approaching the value of AlSi10Mg.
- The percentage of Mg inside the FZ is higher when filler wire is used; however, the obtained value is lower than expected (the wt% content of Mg in the wire is up to 5.5%).

The obtained results in terms of microstructure and microhardness are equally relevant. First of all, the effect of filler wire on hardness within the melt pool could be highlighted, with higher values obtained for both 1_FW and 11_FL samples compared to 9_L by about 30%. This improvement is the result of the higher percentage of Mg (see Table 6) brought on by the chemical composition of the wire, which is in agreement with the literature [31]. Secondly, hardness within the various regions of interest is similar where welding is performed without filler wire, with a maximum percentage difference of 11.5%, confirming homogeneous dilution of AA6082 and AlSi10Mg and a pronounced predominance of AlSi10Mg. This latter conclusion is supported by the high silicon content within the sample, the mean hardness being closer to that of AlSi10Mg and the higher castability of this alloy in comparison to AA6082. On the contrary, samples welded with filler wire exhibit significant differences between peak hardness due to the chemical composition of the wire and the hardness within the HAZ due to poor dilution of the base metal with the wire in the melt pool. Additionally, no improvements in dilution were observed in terms of chemical or mechanical properties when beam wobbling was introduced. However, this lack of homogeneity leads to increased hardness, which together with the weld morphology and low porosity of the sample leads to a weld that is highly resistant under FW conditions. During tensile-shear tests, welding of the sheets under these conditions led to the highest value of failure load ($5.9 \text{ kN} \pm 0.37$) and the equivalent US ($204 \text{ MPa} \pm 9.8$). In general, all welded samples were characterized by a lower US than pure AA6082 and AlSi10Mg. This outcome was to be expected due to the low number of defects in the base material, with porosity completely absent or less than 0.2% in the case of LPBF printed samples. Despite the highest value being obtained under FW conditions, similar mean US values were achieved under other welding conditions. As a result, the contribution of Mg toward increasing the US cannot be completely ruled out, since evidence from manufacturing favored process conditions with filler wire (FL and FW) rather than without (L). While the chemical composition and increased hardness did not seem

to play a fundamental role, the quantity and dimensions of defects had a noticeable and detrimental effect. In fact, FL conditions led to the production of samples exhibiting more brittle behavior than FW, confirming observations in relation to fracture surfaces.

5 Conclusion

The present study has examined the welding of dissimilar aluminum alloy sheets both with and without filler wire while employing linear scanning and laser beam wobbling. Welding of 1.5 mm thick 6082 sheet produced by conventional hot rolling to 4 mm AlSi10Mg produced by LPBF was performed in a lap-joint configuration. In order to find the welding configuration with the required strength, fewest defects, and appropriate morphology, several experiments were conducted in different configurations while varying process parameters. The resulting joints were characterized in terms of microstructure, chemical composition, geometry, and mechanical strength. Defects were minimized (porosity < 2%) with filler wire and wobbling (FW), as well as with linear motion (L). Optimum process parameters were identified for both conditions. Specifically, laser power and welding speed required for high-quality welding were 2200 W and 25 mm/s in the FW configuration and 2000 W and 35 mm/s in the L configuration, highlighting the beneficial effect of linear motion on productivity. The choice of process setup also influenced the morphology of the weld bead. A minimum aspect ratio of 0.34 was obtained with FW welding, while a maximum value of 0.67 was achieved in the L configuration. The addition of filler wire and activation of beam wobbling were strongly correlated with the chemical composition and elemental distribution within the FZ and HAZ interface region. The use of filler wire led to greater chemical anisotropy of the joint, while beam wobbling did not improve homogenization. Furthermore, the higher percentage of Mg in FW welding increased the mean hardness of the joint; however, the fracture surface corresponded to a Mg-free area, so this element had no relevant impact on the strength of the joint. Conversely, porosity had a greater impact on joint strength than any other factor, for which welding in a FW configuration led to the highest strength.

Welding with filler wire and wobbling motion therefore enables joining of hybrid aluminum sheets with a broad process window, achieving the lowest porosity and the highest mechanical strength; however, linear welding may also be a viable option for achieving high productivity despite the fact that it requires more precise process optimization to prevent defects. Higher productivity (35 mm/s for L vs. 25 mm/s for FW) and a simpler process setup may therefore be an attractive option for industrial applications despite a slight reduction in mechanical strength.

Author contributions All authors contributed to the study conception and design. Material preparation, investigation, and analysis were performed by Erica Liverani and Alessandro Ascari with Alessandro Fortunato supervision. The first draft of the manuscript was written by Erica Liverani and all authors commented on previous versions of the manuscript. All authors read and approved the final manuscript.

Funding Open access funding provided by Alma Mater Studiorum - Università di Bologna within the CRUI-CARE Agreement.

Declarations

Competing interests The authors declare no competing interests.

Open Access This article is licensed under a Creative Commons Attribution 4.0 International License, which permits use, sharing, adaptation, distribution and reproduction in any medium or format, as long as you give appropriate credit to the original author(s) and the source, provide a link to the Creative Commons licence, and indicate if changes were made. The images or other third party material in this article are included in the article's Creative Commons licence, unless indicated otherwise in a credit line to the material. If material is not included in the article's Creative Commons licence and your intended use is not permitted by statutory regulation or exceeds the permitted use, you will need to obtain permission directly from the copyright holder. To view a copy of this licence, visit <http://creativecommons.org/licenses/by/4.0/>.

References

- Hausfather Z (2020) How electric vehicles help to tackle climate change, Carbon brief. <https://www.carbonbrief.org/factcheck-how-electric-vehicles-help-to-tackle-climate-change/>. Accessed July 2023
- Kogel-Hollacher M (2020) The full potential of photonics in e-mobility: an overview. *Laser User* 97:22–23
- European Technology and Innovation Platform (2020) strategic research agenda for batteries. <https://ec.europa.eu/newsroom/ener/items/696024/en>. Accessed July 2023
- Chianese G, Franciosa P, Nolte J, Ceglarek D, Patalano S (2022) Characterization of photodiodes for detection of variations in part-to-part gap and weld penetration depth during remote laser welding of copper-to-steel battery tab connectors. *J Manuf Sci Eng* 144(7):071004. <https://doi.org/10.1115/1.4052725>
- Anwar Sattar DG, Greenwood D, Dowson M, Unadkat P (2020) Automotive lithium-ion battery recycling in the UK WMG. Faraday Institute Report. University of Warwick
- Wang L, Rong Y (2022) Review on processing stability, weld defects, finite element analysis, and field assisted welding of ultra-high-power laser (≥ 10 kW) welding. *Int J Hydromech* 5(2):167–190. <https://doi.org/10.1504/IJHM.2022.123135>
- Li H, Ren H, Liu Z, Huang F, Xia G, Long Y (2022) In-situ monitoring system for weld geometry of laser welding based on multi-task convolutional neural network model. *Measurement* 204:112138. <https://doi.org/10.1016/j.measurement.2022.112138>
- Hong K, Shin Y (2017) Prospects of laser welding technology in the automotive industry: a review. *J Mater Proc Technol* 245:46–49. <https://doi.org/10.1016/j.jmatprotec.2017.02.008>
- Moller B, Schnabel K, Wagener R, Kaufmann H, Melz T (2020) Fatigue assessment of additively manufactured AlSi10Mg laser beam welded to rolled EN AW-6082-T6 sheet metal. *J Fatigue* 140:105805. <https://doi.org/10.1016/j.ijfatigue.2020.105805>
- Dimatteo V, Liverani E, Ascari A, Fortunato A (2022) Weldability and mechanical properties of dissimilar laser welded aluminum alloys thin sheets produced by conventional rolling and additive manufacturing. *J Mater Proc Technol* 302:117512. <https://doi.org/10.1016/j.jmatprotec.2022.117512>
- Grünenwald S, Kujanpää V, Salminen A (2007) Nd:YAG laser welding of 5083 aluminium alloy using filler wire. Proceedings of the international laser safety conference. ICALEO® 2007: 26th international congress on laser materials processing, laser micro-processing and nanomanufacturing. Cincinnati, Ohio, USA. (pp. 1002). ASME. <https://doi.org/10.2351/1.5060979>
- Pinto LA, Quintino L, Miranda RM, Carr P (2010) Laser welding of dissimilar aluminium alloys with filler materials. *Weld World* 54:R333–R341. <https://doi.org/10.1007/BF03266747>
- Alshaer AW, Li L, Mistry A (2017) Effect of filler wire properties on porosity formation in laser welding of AC-170PX aluminium alloy for lightweight automotive component manufacture. *Proc Inst Mech Eng , Part B: J Eng Manuf* 231(6):994–1006. <https://doi.org/10.1177/0954405415578584>
- Hagenlocher C, Weller D, Weber R, Graf T (2018) Reduction of the hot cracking susceptibility of laser beam welds in AlMgSi alloys by increasing the number of grain boundaries. *Sci Technol Weld Join* 24:313–319. <https://doi.org/10.1080/13621718.2018.1534775>
- Weller D, Bezençon C, Stritt P, Weber R, Graf T (2013) Remote laser welding of multi-alloy aluminum at close-edge position. *Phys Proc* 41:164–168. <https://doi.org/10.1016/j.phpro.2013.03.065>
- Sokoluk M, Yuan J, Pan S, Li X (2021) Nanoparticles enabled mechanism for hot cracking elimination in aluminum alloys. *Metall Mater Trans A* 52:3083–3096. <https://doi.org/10.1007/s11661-021-06302-9>
- Sokoluk M, Cao C, Pan S, Li X (2019) Nanoparticle-enabled phase control for arc welding of unweldable aluminum alloy 7075. *Nat Commun* 10:98. <https://doi.org/10.1038/s41467-018-07989-y>
- Mohan A, Ceglarek D, Auinger M (2022) Numerical modelling of thermal quantities for improving remote laser welding process capability space with consideration to beam oscillation. *Int J Adv Manuf Technol* 123:761–782. <https://doi.org/10.1007/s00170-022-10182-7>
- Wang L, Gao M, Zhang C, Zeng X (2016) Effect of beam oscillating pattern on weld characterization of laser welding of AA6061-T6 aluminum alloy. *Mater Des* 108:707–717. <https://doi.org/10.1016/j.matdes.2016.07.053>
- Fetzer F, Sommer M, Weber R, Weberpals JP, Graf T (2018) Reduction of pores by means of laser beam oscillation during remote welding of AlMgSi. *Optics Lasers Eng* 108:68–77. <https://doi.org/10.1016/j.optlaseng.2018.04.012>
- Chen L, Mi G, Zhang X, Wang C (2021) Effects of sinusoidal oscillating laser beam on weld formation, melt flow and grain structure during aluminum alloys lap welding. *J Mater Proc Technol* 298:117314. <https://doi.org/10.1016/j.jmatprotec.2021.117314>
- Li L, Gong J, Xia H, Peng G, Hao Y, Meng S, Wang J (2020) Influence of scan paths on flow dynamics and weld formations during oscillating laser welding of 5A06 aluminum alloy. *J Mater Res Technol* 11:19–32. <https://doi.org/10.1016/j.jmrt.2020.12.102>
- Zhang C, Li X, Gao M (2020) Effects of circular oscillating beam on heat transfer and melt flow of laser melting pool. *J Mater Res Technol* 9:9271–9282. <https://doi.org/10.1016/j.jmrt.2020.06.030>
- Schultz V (2019) Process stability during laser beam welding with beam oscillation and wire feed. *J Manuf Mater Proc* 3(1):17. <https://doi.org/10.3390/jmmp3010017>
- Tonelli L, Liverani E, Di Egidio G, Fortunato A, Morri A, Ceschini L (2023) On the role of microstructure and defects in the room and high-temperature tensile behavior of the PBF-LB A357 (AlSi7Mg) alloy in As-built and peak-aged conditions. *Materials* 16(7):2721. <https://doi.org/10.3390/ma16072721>

26. Limbasiya N, Jain A, Soni H, Wankhede V, Krolczyk G, Sahlot P (2022) A comprehensive review on the effect of process parameters and post-process treatments on microstructure and mechanical properties of selective laser melting of AlSi10Mg. *J Mater Res Technol* 21:1141–1176. <https://doi.org/10.1016/j.jmrt.2022.09.092>
 27. Padovano E, Badini C, Pantarelli A, Gili F, D’Aiuto F (2020) A comparative study of the effects of thermal treatments on AlSi10Mg produced by laser powder bed fusion. *J Alloys Compounds* 831:154822. <https://doi.org/10.1016/j.jallcom.2020.154822>
 28. Sánchez-Amaya JM, González-Rovira L, Botana FJ (2009) Laser welding of aluminium alloys 5083 and 6082 under conduction regime. *Appl Surface Sci* 255:9512–9521. <https://doi.org/10.1016/j.apsusc.2009.07.081>
 29. Fetzter F, Hagenlocher C, Weber R, Graf T (2021) Geometry and stability of the capillary during deep-penetration laser welding of AlMgSi at high feed rates. *Optics Laser Technol* 133:106562. <https://doi.org/10.1016/j.optlastec.2020.106562>
 30. Wang X, Lu F, Wang H, Qu Z, Xia L (2016) Micro-scale model based study of solidification cracking formation mechanism in Al fiber laser welds. *J Mater Proc Technol* 231:18–26. <https://doi.org/10.1016/j.jmatprotec.2015.12.006>
 31. Yuan J, Liu Q, Pan S, Li J, Murali N, Wang S, Li X (2022) Nano-treating promoted solute dissolution for novel high strength Al-Cu-Mg alloys. *Materialia* 24:101466. <https://doi.org/10.1016/j.mtla.2022.101466>
- Publisher’s note** Springer Nature remains neutral with regard to jurisdictional claims in published maps and institutional affiliations.